

# VISRAD – A 3-D View Factor Code and Design Tool for High Energy Density Physics Experiments

J. J. MacFarlane  
Prism Computational Sciences  
455 Science Drive, Suite 140  
Madison, WI 53711  
jjm@prism-cs.com

## **Abstract**

The 3-D view factor code VISRAD is used to both design high energy density physics (HEDP) experiments, and to simulate the multi-dimensional radiation environment within target systems; *i.e.*, hohlraums and associated components such as diagnostic holes, capsules, and backlighters. VISRAD target systems are built using a variety of geometric primitives, and surface removal algorithms (*e.g.*, drilling holes in cylinders) can be employed to build complex targets. Laser beam parameters – power profiles, pointing, and focusing – can be specified for either individual beams or groups of beams. At present, the OMEGA and NIF laser systems are supported by VISRAD. The use of multiple coordinate systems is supported so that target components can be positioned and oriented, and laser beams can be pointed, in the target chamber coordinate system or in the coordinate system of any target component. Radiation flux distributions about the target system are computed by solving a coupled set of power balance equations in which the emission from a given surface element in the target grid is coupled to all other surface elements. Accurate algorithms are used in computing the configuration (view factor) integrals. At any point in the grid, the time- and frequency-dependent flux incident onto that point can be viewed and/or written to a file to be used as input to radiation-hydrodynamics simulations. Energy source models include laser energy deposition – computed using 3-D ray-trace algorithms – and self-radiating target components. To aid designers in setting up targets, pointing beams, and viewing results, VISRAD has an easy-to-use graphical user interface and interactive 3-D graphics. The code has been designed for cross-platform use on Windows, Unix, and Mac OS X platforms.

Keywords: View factor, radiation flux, ICF, radiation

## INTRODUCTION

Designing high energy density physics (HEDP) experiments at large facilities – such as the OMEGA facility at the University of Rochester, the National Ignition Facility (NIF) currently being built at Lawrence Livermore National Laboratory, and the Z high-current z-pinch facility at Sandia National Laboratories – presents a variety of challenges. For laser systems with many beams, experimental design issues can arise due to the complex 3-D geometries associated with beam–target–diagnostics orientations. Such issues include laser beam pointing, target and backlighter positioning, location of diagnostic holes in target components, alignment of diagnostics, and addition of shields designed to eliminate unwanted photons from contaminating measurements. Proper planning and design of experiments is especially important for experiments at large facilities not only because of the high costs per shot, but also because the mispointing of high-power laser beams can potentially damage laser optics or target chamber components.

For experiments involving hohlraums, another important aspect of designing experiments is predicting the radiation environment within the hohlraum, and designing target systems (*i.e.*, hohlraums and associated components such as diagnostic holes, capsules, backlighters) to produce optimum conditions for a particular investigation. For example, for experiments designed to study the response of materials to intense radiation fields, it may be important to design the experiment so that the incident radiation flux onto the sample is spatially uniform. Alternatively, it may be necessary to maximize the radiation temperature within a hohlraum. Further, for inertial confinement fusion (ICF) experiments, it may be desirable to optimize the symmetry of radiation incident onto a capsule.

VISRAD is a 3-D view factor and experimental design code that is used in designing – and analyzing data from – high energy density plasmas experiments. It is used for experiments at OMEGA [1-3], at Z [4-8], and will soon be used to design experiments at NIF. Designers can use VISRAD to “build” targets, orient them within target chambers, point laser beams, check beam-target interactions, and view diagnostic lines-of-sight. In addition, it can compute the radiation environment within hohlraums, and can simulate the time- and frequency-dependent radiation field incident onto any surface element in the target

system. To aid designers, it includes a graphical user interface and interactive 3-D graphics for setting up problems and displaying results.

In this paper, we describe some of the major features of VISRAD, and present two example applications: (1) hohlraum experiments at OMEGA designed to study the properties of radiatively-heated ablator samples, and (2) experiments at the Z facility designed to study the heating of materials by intense x-ray radiation. Details concerning the calculation of configuration (view factor) integrals are provided in an appendix.

### MAJOR FEATURES OF VISRAD

VISRAD has been developed to model radiation environments in HEDP experiments, and to facilitate the design of experiments. It provides both a CAD/graphics capability for building target systems and pointing laser beams, and a view factor capability to simulate the radiation flux distribution about a target system. Unlike multi-dimensional radiation-hydrodynamics codes, it does not compute the movement and heating of plasmas based on plasma/atomic processes and the solution of numerical differential equations for energy and momentum conservation. Rather, it is a convenient easy-to-use tool for studying a variety of issues relevant to the successful performance of HEDP experiments.

Target systems are composed of one or more target components, or *objects*. Target components in turn are composed of *surface elements*. In a typical application there may be several hundred to several thousand surface elements.

Radiation fluxes throughout a target system are determined from a coupled set of steady-state power balance equations (see, e.g., Ref. 9). Thus, the flux distribution at any given time is independent of any other time. However, VISRAD supports performing multi-timestep simulations in which laser powers and target component sizes, albedos, x-ray conversion efficiencies, and radiative self-emission change with time. Users can specify the time-dependence of any of these parameters in several ways: table entry, reading in data from (multi-column ASCII) files, or user-specified analytic expressions. This multi-timestep option

provides a convenient means of generating time-dependent data for other applications (*e.g.*, input for radiation-hydrodynamics codes).

In computing configuration factor (or *view factor*) integrals and solving radiosity equations, VISRAD utilizes algorithms originally developed for SYMRAD [10,11]. These algorithms have been extensively benchmarked against analytic solutions, results from other view factor codes, and HEDP experiments [10].

### *Target Setup*

Targets can be built using a variety of geometric primitives, including spheres, cylinders, cones, disks, rectangles, boxes, spokes, cylindrical hohlraums and halfraums, spherical tetrahedral hohlraums, and cylindrical slotted hohlraums. For several of these (spheres, cylinders, cones, disks) all or a portion of the component can be utilized. Surface removal is also supported in VISRAD. That is, portions of any target component, or “object,” can be removed using cylindrical or box clipping volumes. This allows designers to generate, for example, cylindrical hohlraums with diagnostic holes. Objects can be positioned using the target chamber coordinate system or the coordinate system of any other target component. Material properties are specified on an object-by-object basis. Material properties include albedo, x-ray conversion efficiency, and radiating power (self-emission). Both material properties and object sizes may be time-dependent or constant.

### *Supported Experimental Facilities*

VISRAD currently supports the design and simulation of experiments at the OMEGA 60-beam laser facility at the University of Rochester, the National Ignition Facility (NIF) currently being built at Lawrence Livermore National Laboratory (192 laser beams are anticipated), and the Z high-current z-pinch facility at Sandia National Laboratories. Data for OMEGA and NIF laser and diagnostic port positions are stored in VISRAD, allowing the experiment designer to easily view the target system from any diagnostic port or

user-specified position. The positions of the laser and diagnostic ports can be displayed in the coordinate system of any of the target components, as well as the target chamber.

VISRAD can also be used to model the effects of unconverted laser light ( $\lambda = 1.05 \mu\text{m}$  and  $\lambda = 0.53 \mu\text{m}$ ) in NIF experiments. This can be important because a significant amount of  $\lambda = 1.05 \mu\text{m}$  and  $\lambda = 0.53 \mu\text{m}$  light enters the chamber, and this light is focussed to points that are offset tens of cm from the  $\lambda = 0.35 \mu\text{m}$  focus for each beam [12]. This is illustrated in Figure 1, which shows an example in which the four beams from a single NIF quad, *i.e.*, a group of four laser beams, are pointed such that the blue ( $\lambda = 0.35 \mu\text{m}$ ) light is focussed to a point at the surface of a rectangular foil. Also, shown in the image is unconverted red ( $\lambda = 1.05 \mu\text{m}$ ) light, which focuses to a point 46 cm beyond the  $\lambda = 0.35 \mu\text{m}$  focus. Similarly, the green ( $\lambda = 0.53 \mu\text{m}$ ) light focuses to a point between the  $\lambda = 0.35 \mu\text{m}$  and  $\lambda = 1.05 \mu\text{m}$  focus points. By computing the laser power density deposited across the target, it is possible to assess whether the unconverted laser light could have a negative impact on the experiment.

Options for modeling spatial smoothing effects due to phase plates at OMEGA are also included. This includes SG3 distributed phase plates (DPP) with and without polarization smoothing, and SG8 DPP [13]. For all laser systems, laser beam parameters can be specified individually or by cluster (*i.e.*, groups of beams). Laser powers can be either time-dependent or constant. Pointing of beams can be done in the coordinate system of the target chamber or any target component.

Laser energy deposition is modeled using a 3-D ray-trace algorithm. In this approach, each beam is divided into a large number ( $\sim 10^2 - 10^4$ ) “beamlets.” Each beamlet has a power determined using both the total power in the beam and the spatial profile of the beam. Each beamlet is treated as a ray, which originates from its beam port near the target chamber wall. The laser power deposited at a surface element is dependent on the number and power of the beamlets that hit that surface element.

### *Flux Distributions*

A coupled set of radiosity equations describes the relationship between the surface emission, absorption, and source terms. It balances the radiative power emitted by a surface element with the power

absorbed by that element and the power from other sources (*e.g.*, laser beams). The radiosity equation for a given surface element  $i$  can be written as:

$$B_i - \mathbf{a}_i \sum_j F_{ij} B_j = Q_i, \quad (1)$$

where  $B_i$  is the “radiosity” of surface  $i$ ,  $\mathbf{a}_i$  is its albedo (or reflectivity),  $Q_i$  is the source term, and  $F_{ij}$  is the occultation-corrected configuration factor [9]. Physically,  $B_i$  is the energy radiated per unit area per unit time from surface  $i$ , and can be written as  $B_i = s T_{e,i}^4$ , where  $T_{e,i}$  is the emission temperature. The total radiative flux going onto surface  $i$  due to radiation from all other surfaces is:

$$q_i^{in} = \sum_j F_{ij} B_j, \quad (2)$$

This can also be used to define a “radiation temperature” at surface  $i$ :  $q_i^{in} = \mathbf{s} T_{R,i}^4$ .

The configuration factors in Eq. (1) depend only on the geometry of the individual surface elements. The source terms are computed using either the laser ray-trace model or target component self-emission model. Given  $Q_i$ ,  $\mathbf{a}_i$ , and  $F_{ij}$ , the radiosity equation is simply a matrix equation which can be inverted to provide  $B_i$  for all surfaces, or alternatively, can be solved using an iterative procedure. Details on computation of the configuration factors,  $F_{ij}$ , are provided in Appendix A. Details describing calculations to benchmark these radiosity algorithms have been presented elsewhere [10].

The frequency-dependent incident flux onto any surface element is obtained by summing the Planckian emission from each surface element:

$$q_i^{in}(\nu) = \sum_j F_{ij} \mathbf{p} B_\nu(T_{e,j}), \quad (3)$$

where  $B_\nu(T_{e,j})$  is the Planck function corresponding to the emission temperature of surface  $j$ . Using this model, the time- and frequency-dependent flux onto any surface element in the target grid can be readily computed. VISRAD provides the option of writing this data to a file, which in turn is used as input to radiation-hydrodynamics simulations.

### *Platforms*

VISRAD has been developed using Qt [14] cross-platform C++ user interface software. It also utilizes OpenGL [15] graphics application framework. The use of Qt and OpenGL allow VISRAD to run on a wide variety of platforms. VISRAD currently runs on the platforms with the following operating systems: MS Windows (NT, 95/98/2000, XP), Macintosh OS X, and Sun Solaris.

## **APPLICATION TO RADIATIVELY-HEATED PLASMA EXPERIMENTS**

To illustrate some of the uses of VISRAD, we present two example applications: (1) an OMEGA hohlraum experiment designed to study radiation propagating into various ablator materials; and (2) radiatively-heated foils exposed to intense z-pinch x-rays at the Sandia Z facility. Both applications are based on experiments performed at these facilities.

### *Hohlraum Experiments at OMEGA*

In performing indirect-drive experiments at OMEGA to study the effects of mid-Z dopants on radiation propagation through doped ablator materials, ablator samples were attached to one end of cylindrical hohlraums, opposite the laser entrance hole (LEH). Fifteen drive beams heated the hohlraum to  $\sim 175$  eV. Time-resolved  $K\alpha$  spectroscopy was used to track the radiation front burning into the ablator samples. A high-Z backlighter was located outside the LEH and heated by 3 overlapping backlighter beams (see Figure 2). For these experiments, VISRAD has been used to:

- determine whether beams used to heat the backlighter might inadvertently hit portions of the hohlraum;
- compute the time-dependent drive temperature seen by the ablator sample and the uniformity of radiation incident on the sample;

- compute the hohlraum emission, or “wall,” temperature and estimate what fraction of the x-rays seen by the x-ray diode array detector (XRD) were due to wall reemission relative to emission from laser hot spots;
- determine which laser beams produced hot spots in the field of view of the XRD’s, and determine the extent to which beam power imbalance can affect the prediction of the drive temperature onto the ablator sample;
- estimate the extent to which the spectrum incident onto the sample was non-Planckian;
- investigate the sensitivity of the incident flux on the ablator sample to laser beam pointing; and
- compute the contribution of the backlighter photons to the overall flux seen by the ablator sample.

Figure 3 shows the sensitivity of the drive temperature at the ablator to the pointing of laser beams in the hohlraum. The beams entered the hohlraum in two cones. Cone 2 contained 5 beams and entered the LEH at an angle of 42.0 degrees, while Cone 3 contained 10 beams entering the LEH at an angle of 58.9 degrees. The solid curve corresponds to calculations in which the beams of both cones are focused to the same point. In this case, the drive temperature at the ablator reaches a maximum of 171 eV when the focus is very close to the plane of the LEH. For calculations in which the beams of Cone 3 focus to a point that is offset 300  $\mu\text{m}$  relative to Cone 2 beams (dotted curve), the peak drive temperature is 175 eV. This occurs where the Cone 3 beams are focussed to a point approximately 200  $\mu\text{m}$  just inside the hohlraum.

Figure 4 shows an example of the calculated incident spectrum onto the ablator sample. Also shown are the individual contributions from the hohlraum (cylinder) and backlighter. The calculations show that only  $\sim 1 - 5\%$  of the total radiation seen by the ablator is due to the backlighter, depending on the photon energy. The dotted curve in Fig. 4 is a Planckian (blackbody) spectrum with the equivalent frequency-integrated flux as the total incident flux onto the sample. The flux seen by the sample at photon energies  $\gtrsim 1$  keV is higher than what would be predicted by a simple Planckian model. (Note, however, that this



spectrum lacks the detailed atomic physics – specifically, that due to M-band emission from a hot Au non-LTE plasma – that is needed to make accurate predictions of the frequency-dependent keV flux.)

Summarizing other results, the VISRAD calculations indicate that the radiation temperature (*i.e.*, the temperature based on the *incident* flux) at the location of the sample is approximately 10 – 15 eV higher than throughout the “barrel” region of the hohlraum wall. Calculated fluxes at the ablator sample were found to be very uniform, with the maximum change in flux (peak-to-valley) across the central 600  $\mu\text{m}$  diameter of the sample typically being only  $\sim 1.4\%$  (or  $\sim 0.35\%$  in radiation temperature).

VISRAD was also used in analyzing hohlraum temperatures based on XRD signals. Here, we found that laser hot spots from four of the beams in our experiments were in the direct field of view of the XRD’s, and approximately 50% of the flux seen by the XRD’s was due to laser hot spots (the other 50% due to wall reemission). Also, when taking into account the beam power imbalance inferred in one of the experiments, the inferred hohlraum temperature decreased by 3 – 4 eV.

#### *Foils Heated by Z-Pinch X-ray Radiation*

Intense z-pinch x-ray sources have been used investigate the radiative heating planar foils [16,17], low-density foams [18], and gases [19,20]. An important component in the analysis of these experiments is the simulation of the time-dependent radiation field onto the experimental sample. Figure 5 shows an illustration of the experimental setup for one of these experiments. In it, the pinch emits x-rays from inside a slotted hohlraum (the slots provide diagnostic access for measuring the pinch properties). Samples located outside the hohlraum are exposed to intense x-ray radiation from the pinch. In these experiments, radiation temperatures at the sample are  $\sim$  several tens of eV. In order to simulate the heating of a sample and analyze data from the experiment, the radiation flux onto the sample must be determined.

Using experimentally measured pinch power and radii, VISRAD is used to compute the time- and frequency-dependent flux onto sample. Figure 6 shows an example of the frequency-dependent incident flux computed for a foil located at a distance of 7.4 cm from the pinch axis. It shows that the incident spectrum is very non-Planckian (compare vs. dotted curve). This is due to the fact that the sample sees both direct

radiation from the pinch, and well as reemitted radiation from the surrounding surfaces. It is important to compute the incident non-blackbody spectrum in analyzing these radiation heating experiments because radiation-hydrodynamics simulations have shown [16] that the heating of the sample is affected by the non-Planckian nature of the incident radiation field.

## SUMMARY

VISRAD is an easy-to-use tool that aids in the design and analysis of HEDP experiments. In its current state, it is being used to design experiments at OMEGA, Z, and NIF. In addition to designing target systems and determining laser pointings and diagnostic lines-of-sight, it is used to compute the 3-D radiation flux distributions throughout target systems. Example applications include:

- Computing the time- and frequency-dependent incident flux onto a sample (*e.g.*, a foil or gas cell) for radiation heating experiments, and writing data to files that are used as input to radiation-hydrodynamics simulations.
- Determining the asymmetry of radiation fields incident on a capsule in indirect-drive ICF experiments.
- Computing hohlraum radiation temperatures.
- Determining the uniformity of laser energy deposition on surfaces (*e.g.*, backlighters, direct-drive cylinders or spheres) where overlap of multiple beams is possible.
- Ensuring that laser beams are hitting/missing intended regions of the target system.
- Computing the radiation reemitted from hohlraum walls, and simulating the radiation field seen by a detector (*e.g.*, an XRD array).
- Predicting the uniformity of incident radiation onto a surface.
- Assessing the effects of beam imbalance in laser experiments.

Finally, it is expected that development of VISRAD will continue in several areas, including: adding support for additional and/or more flexible laser and diagnostic systems; importing of experimental laser beam data

immediately following experiments for rapid post-shot analyses; and adding capability for displaying a wider variety of results.

## Appendix A. Evaluation of Configuration Factor Integrals

The configuration factor, or view factor, for two finite areas can be written as [9]:

$$F_{ij} = \frac{1}{2p A_i} \int_{A_i} \int_{A_j} \frac{\cos \mathbf{q}_i \cos \mathbf{q}_j}{p S^2} dA_i dA_j \quad (\text{A.1})$$

where  $A_i$  and  $A_j$  are the areas of surfaces  $i$  and  $j$ , respectively,  $S$  is the distance between differential elements  $dA_i$  and  $dA_j$ , and  $\mathbf{q}_i$  ( $\mathbf{q}_j$ ) is the angle between the surface and normal vector of element  $dA_i$  ( $dA_j$ ). Physically,  $F_{ij}$  is the fraction of energy leaving surface  $i$  that arrives at surface  $j$ . The reciprocity relation for configuration factors is:

$$A_i F_{ij} = A_j F_{ji}. \quad (\text{A.2})$$

In our view factor code, we take advantage of the reciprocity relation by computing view factors as follows:

$$\begin{aligned} F_{ij} (i < j) & \text{ are evaluated numerically,} \\ F_{ij} (i = j) & = 0 \quad [\text{due to all surface elements being planar}] \\ F_{ij} (i > j) & = (A_j/A_i) F_{ji}. \end{aligned}$$

In this appendix, we describe methods for evaluating Eq. (A.1). These methods have been benchmarked against each other and known analytic solutions to assess trade-offs in accuracy and computational efficiency. These benchmark calculations are described in [10].

By applying Stoke's theorem [9], we can replace the quadruple integral (*i.e.*, two areal integrals) in Eq. (A.1) with a double contour integral, which can be written as:

$$F_{ij} = \frac{1}{2p A_i} \oint_{C_i} \oint_{C_j} \left( \ln S dx_j dx_i + \ln S dy_j dy_i + \ln S dz_j dz_i \right) \quad (\text{A.3})$$

Thus, the integral over two areas is replaced by integrals over the boundaries about the two surfaces (see Figure A.1). This allows for considerable savings in computer time [21]. In the example shown in Figure A.1, the double contour integral represents the sum of 16 segment-to-segment combinations (the boundary of each quadrilateral is composed for 4 segments).

### Evaluation of Individual Segment-to-Segment Combinations

Let us define:

$$\mathbf{g}_{ab} = \int_{A_a}^{B_a} \int_{A_b}^{B_b} \ln S (dx_a dx_b + dy_a dy_b + dz_a dz_b), \quad (\text{A.4})$$

where  $A_a$  and  $B_a$  define the end points of segment  $\mathbf{s}_a$ , which has length  $L_a$ , and  $A_b$  and  $B_b$  define the end points of segment  $\mathbf{s}_b$ , which has length  $L_b$ . In Eq. (A.4), the distance between points on the segments,  $S$ , varies as we move along each segment. The total configuration factor is then:

$$F_{ij} = \frac{1}{2pA_i} \sum_a \sum_b \mathbf{g}_{a_b}. \quad (\text{A.5})$$

We next apply a coordinate transformation to locate one of the segments along the  $z$ -axis and place one of its end points at the origin (see Fig. A.2(b)). Then Eq. (A.4) becomes:

$$\mathbf{g}_{ab} = \int_0^{L_a} dz_a \int_{z_b^0}^{z_b^1} dz_b \ln S. \quad (\text{A.6})$$

Note that the first two terms of Eq. (A.4) can be dropped because segment  $\mathbf{s}_a$  is parallel to the  $z$ -axis. We write the integrand as:

$$\ln S = \frac{1}{2} \ln [x_b^2 + y_b^2 + (z_b - z_a)^2]. \quad (\text{A.7})$$

Next we define  $t_a = z_a / L_a$  and  $t_b = (z_b - z_{b0}) / \Delta z_b$ , where  $\Delta z_b = z_{b1} - z_{b0}$  (see Fig. A.2). We then have:

$$\mathbf{g}_{a_b} = \frac{L_a \Delta z_b}{2} \int_0^1 dt_b \int_0^1 dt_a \ln [S(t_a, t_b)^2]. \quad (\text{A.8})$$

Note that  $t_a$  and  $t_b$  represent the fractional distance moved along segments  $\mathbf{a}$  and  $\mathbf{b}$ , respectively. At this point,  $\mathbf{g}_{ab}$  can be evaluated numerically by performing the double integration:

$$\mathbf{g}_{a_b} = \frac{L_a \Delta z_b}{2} \sum_k^{N_a} \mathbf{w}_k \sum_j^{N_b} \mathbf{w}_j \ln[S(t_j, t_k)^2], \quad (\text{A.9})$$

where  $\mathbf{w}_k$  and  $\mathbf{w}_j$  are integration weights. This method, which is typically used in view factor codes [21,22], is easily performed by breaking segments  $\mathbf{a}$  and  $\mathbf{b}$  into  $N_a$  and  $N_b$  sub-segments.

Significant additional accuracy – as well as computational efficiency in many cases – can be obtained by performing an analytic integration of the inside integral in Eq. (A.8). To do this, we define:

$$I_1(t_b) = \int_0^1 dt_a \ln[S(t_a, t_b)^2]. \quad (\text{A.10})$$

Noting that:

$$S^2 = x_b^2 + y_b^2 + (z_b - z_a)^2 = a + bt_a + ct_a^2, \quad (\text{A.11})$$

where

$$a = [x_b(t_b)]^2 + [y_b(t_b)]^2 + [z_b(t_b)]^2$$

$$b = -2L_a z_b(t_b)$$

$$c = L_a^2,$$

and

$$x_b(t_b) = x_{b0} + t_b \Delta x_b; \quad \Delta x_b = x_{b1} - x_{b0}$$

$$y_b(t_b) = y_{b0} + t_b \Delta y_b; \quad \Delta y_b = y_{b1} - y_{b0}$$

$$z_b(t_b) = z_{b0} + t_b \Delta z_b; \quad \Delta z_b = z_{b1} - z_{b0},$$

we have:

$$I_1(t_b) = (1 + \frac{b}{2c}) \ln[a + b + c] - \frac{b}{2c} \ln[a] - 2 + \frac{q}{c} [\tan^{-1}(\frac{2c+b}{q}) - \tan^{-1}(\frac{b}{q})], \quad (\text{A.12})$$

where  $a$  and  $b$ , as indicated above, are functions of  $t_b$ , and  $q = (4ac - b^2)^{\frac{1}{2}}$ . Eq. (A.8) then becomes:

$$\mathbf{g}_{ab} = \frac{L_a \Delta z_b}{2} \sum_k^{N_b} \mathbf{w}_k I_1(t_k). \quad (\text{A.13})$$

Additional accuracy can be achieved by evaluating the remaining integral analytically for the first three terms of  $I(t_b)$  in Eq. (A.12). Integrating over the first three terms in Eq. (A.12), and reorganizing the last two ( $\tan^{-1}$ ) terms, we obtain:

$$\mathbf{g}_{ab} = \frac{L_a \Delta z_b}{2} I_2 + \Delta z_b \int_0^1 dt_b r_b (\mathbf{s} + \mathbf{q}), \quad (\text{A.14})$$

where

$$\begin{aligned} I_2 = & -2 - 2\mathbf{r} + \mathbf{h}(1-2h) + \ln(\Omega L_b^2 + (1+2h)L_b^2) [\mathbf{r}(1+h) + \mathbf{h}(1+\Omega - 2h^2)] \\ & + \ln(\Omega L_b^2) [\mathbf{r}h - \mathbf{h}(1+\Omega - 2h^2)] + \mathbf{e}(\mathbf{r} + 2\mathbf{h}h) [\tan^{-1}(2(1+h)/\mathbf{e}) - \tan^{-1}(2h/\mathbf{e})] \end{aligned}$$

and

$$\mathbf{r} = 1 - (z_b / L_a)$$

$$\mathbf{h} = \Delta z_b / (2L_a)$$

$$h = [x_{b0} \Delta x_b + y_{b0} \Delta y_b + (z_{b0} - 2L_a) \Delta z_b] / L_b^2$$

$$\Omega = [x_{b0}^2 + y_{b0}^2 + (z_{b0} - L_a)^2] / L_b^2$$

$$\mathbf{e} = 2(\Omega - h^2)^{1/2}$$

$$\mathbf{q} = \tan^{-1}(z_b / r_b)$$

$$\mathbf{s} = \tan^{-1}((L_a - z_b) / r_b)$$

$$z_b = z_{b0} + t_b (z_{b1} - z_{b0})$$

and

$$r_b = [(x_{b0} + t_b \Delta x_b)^2 + (y_{b0} + t_b \Delta y_b)^2]^{1/2}$$

Benchmark calculations in which evaluation of configuration factors was performed using Eq. (A.14) showed that in most test problems this method provided both superior accuracy and least CPU solution times compared to other techniques (*e.g.*, see Eq. (A.9)).

Finally, a significantly simpler technique for computing configuration factors is given by:

$$F_{ij} = - \frac{1}{2\rho A_i} \frac{2A_i A_j}{S^4} (\hat{n}_i \cdot \vec{r}) (\hat{n}_j \cdot \vec{r}). \quad (\text{A.15})$$

where  $\vec{r}$  is the vector from the centroid of surface  $i$  to the centroid of surface  $j$ ,  $S = |\vec{r}|$ , and  $\hat{n}_i$  and  $\hat{n}_j$  are the unit normal vectors of surfaces  $i$  and  $j$ , respectively. Solutions using this method tend to be less accurate than other approaches, but improve in accuracy as the separation between surfaces  $i$  and  $j$  becomes large. Sometimes referred to as the “five times rule” [23], an accuracy of  $\leq 2.5\%$  can be expected when the surfaces are separated by at least 5 surface element diameters, and  $\leq 0.1\%$  when the surfaces are separated by at least 20 diameters.



## REFERENCES

- [1] Batha, S. H., Barnes, C. W., Christensen, C. R., *Rev. Sci. Instrum.*, in press (2002).
- [2] MacFarlane, J. J., Cohen, D. H., Penrose, K. L., Connors, D., Haynes, D. A., *Simulation of Hohlraum Radiation Environments*, presented at the 2<sup>nd</sup> International Conference on Inertial Fusion Sciences and Applications, Kyoto, JP (2001).
- [3] Workman, J. B., Los Alamos National Laboratories, private communication (2002).
- [4] Peterson, R. R., *et al.*, submitted to *Phys. Plasmas* (2001).
- [5] Rochau, G. A., *et al.*, Absorption Spectroscopy of Al Tracers in Low-Density CH Foam Heated by Z-Pinch Radiation, presented at the 14th Topical Conference on High Temperature Plasma Diagnostics, Madison, WI (2002).
- [6] Cohen, D. H., MacFarlane, J. J., Bailey, J. E., Liedahl, D. A., *Rev. Sci. Instrum.*, in press (2002).
- [7] Woodruff, P. R., MacFarlane, J. J., Cohen, D. H., Penrose, K. L., Connors, D., Haynes, D. A., Analysis of a Strongly Coupled NaF Plasma Produced by Z-Pinch Radiation, presented at the 14th Topical Conference on High Temperature Plasma Diagnostics, Madison, WI (2002).
- [8] MacFarlane, J. J., *et al.*, Simulation of the Radiative Heating of Gold-Backed Thin Foils in Z-Pinch Experiments, presented at the 5th International Conference on Dense Z-Pinches, Albuquerque, NM (2002).
- [9] Siegel, R., Howell, J. R., *Thermal Radiation Heat Transfer*, Third Edition, Hemisphere Publishing, Washington, DC (1992).
- [10] MacFarlane, J. J., Development of a Time-Dependent View Factor Code for Studying Radiation Symmetry in ICF Hohlraums, University of Wisconsin Report, UWFD-1061 (1998).
- [11] MacFarlane, J. J., *et al.*, *Rev. Sci. Instrum.* 72, 1228 (2001).
- [12] Kalantar, D., private communication (2002). See also Dixit, S. N., *et al.*, Lawrence Livermore National Laboratory Report UCRL-LR-105821-91-1 (1998).
- [13] Regan, S. P., private communication (2001).

- [14] Qt is a product of Trolltech, AS, Oslo, Norway.
- [15] Woo, M., Nieder, J., Davis, T., OpenGL Programming Guide, Addison-Wesley, Reading, MA (1997).
- [16] MacFarlane, J. J., *et al.*, Phys. Rev. E, in press (2002).
- [17] Bailey, J. E., *et al.*, JQSRT (2001).
- [18] Rochau, G. A., *et al.*, presented at the 14th Topical Conference on High Temperature Plasma Diagnostics, Madison, WI (2002).
- [19] Bailey, J. E., *et al.*, Phys. Plasmas, in press (2002).
- [20] Cohen, D. H., *et al.*, Rev. Sci. Instrum., in press (2002).
- [21] Gorel, C. M., Torrance, K. E., Greenberg, D. P., Battaile, B., Computer Graphics 18, 213 (1984).
- [22] Drake, D. J., J. Comp. Phys. 87, 73 (1990).
- [23] Baum, D. R., Rushmeier, H. E., Winget, J. M., Computer Graphics 23, 325 (1989).

## FIGURE CAPTIONS

Figure 1: VISRAD image of NIF beams from Q15T quad irradiating a rectangle oriented perpendicular to the centroid of the incoming beams. The beams are pointed such that the  $3\omega$  light (shown in olive) is focussed at the center of the rectangle. Unconverted  $1\omega$  light is shown by the red cones. ( $2\omega$  light is not shown for clarity.) The spatial distribution of the source power due to laser deposition is shown as color contours on the rectangle. The size of the rectangle is 3 cm x 6 cm. The view is from NIF Port 7 –240.

Figure 2. Left: VISRAD image of laser beams irradiating backlighter. High-Z backlighter is mounted on a rectangular support. Ablator sample is mounted at end of hohlraum, opposite LEH, and covered with a washer (for aperturing). Right: VISRAD image showing drive beams entering hohlraum. Drive beams all have clear path to LEH without interference by the backlighter. The small yellow rectangle on the left side of the image is a 1 mm x 1 mm square representing the XRD detector. [Note images are shown using perspective (non-orthographic) projection.]

Figure 3. Calculated drive temperatures as a function of laser pointing for an ablator patch located at one end of a cylindrical hohlraum. Fifteen laser beams enter hohlraum in two cones. Higher drive temperatures are achieved when cones are offset by  $\sim 300 \mu\text{m}$ .

Figure 4. Calculated incident flux as a function of photon energy. Solid: total flux. Dashed: contribution due to hohlraum. Dash-dotted: contribution due to backlighter. Dotted: Planckian spectrum with same frequency-integrated flux as total.

Figure 5. VISRAD grid for modeling radiation heating experiments at Z. A foil located at a radius of 7.4 cm is shown in the upper right portion. Color contours correspond to the radiation temperature ( $sT_R^4 = F^{in}$ ).

Figure 6. Solid: Frequency-dependent incident radiation flux calculated for a sample located 7.4 cm away from the pinch axis. Dotted: blackbody spectrum for equivalent frequency-integrated flux.

Figure A.1. Two surface elements illustrating contour integration technique.

Figure A.2. Illustrations showing segment-to-segment couplings for contour integration solution of configuration factor integrals. (a) Original coordinate system. (b) Transformed coordinate system.

Figure 1.

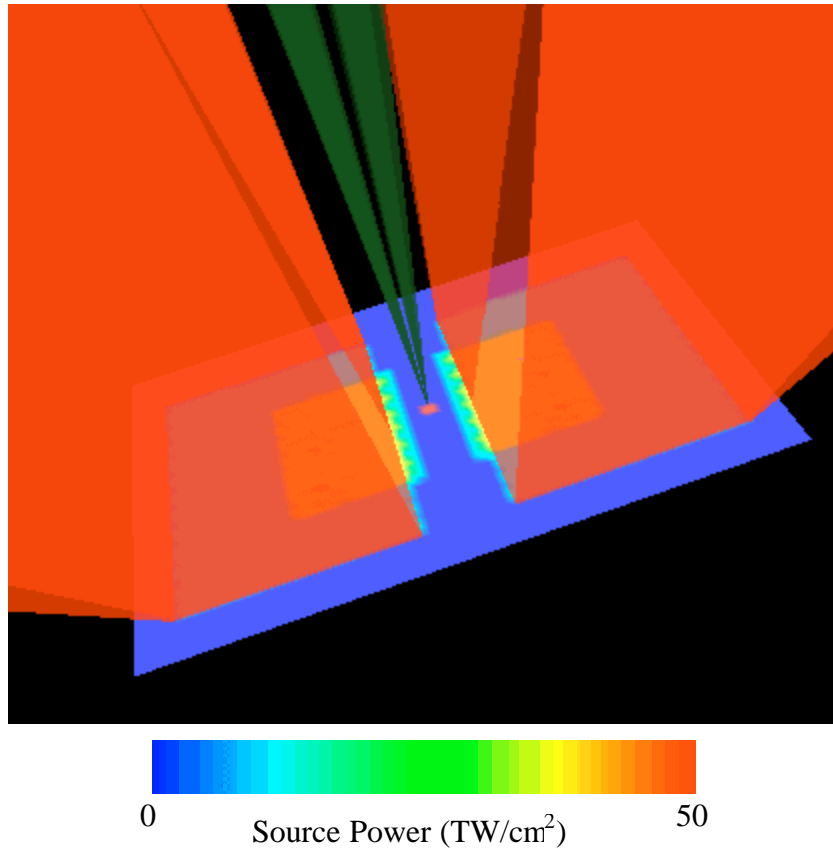


Figure 2.

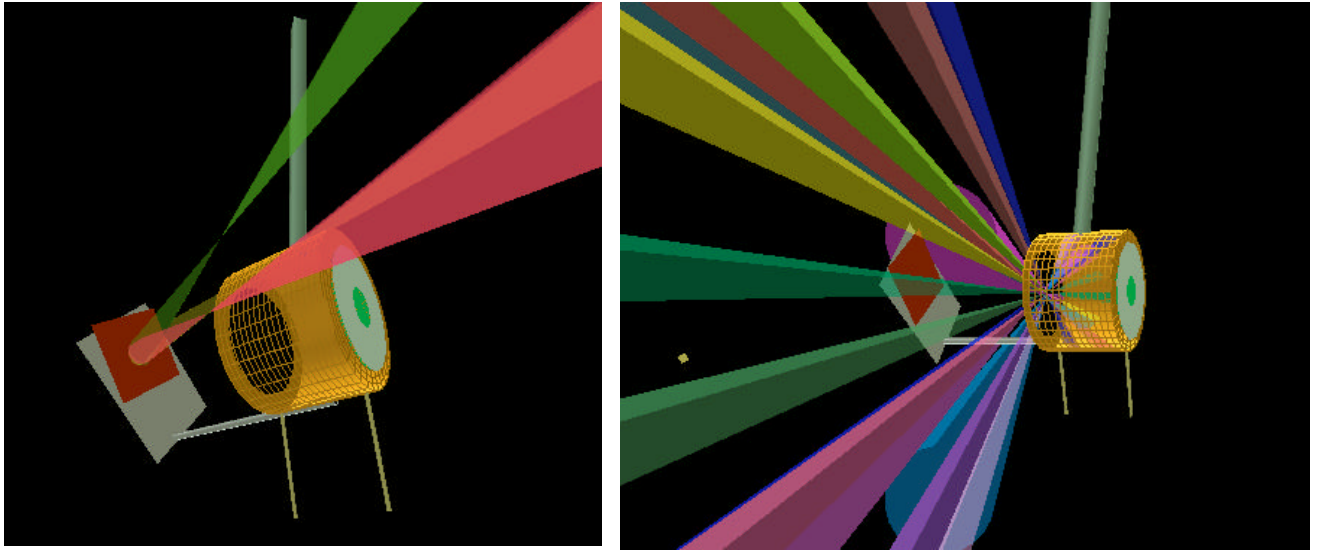


Figure 3.

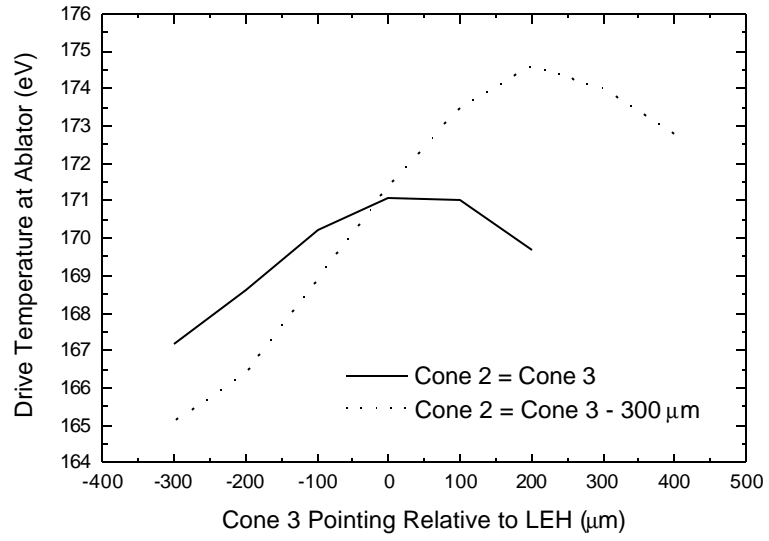


Figure 4.

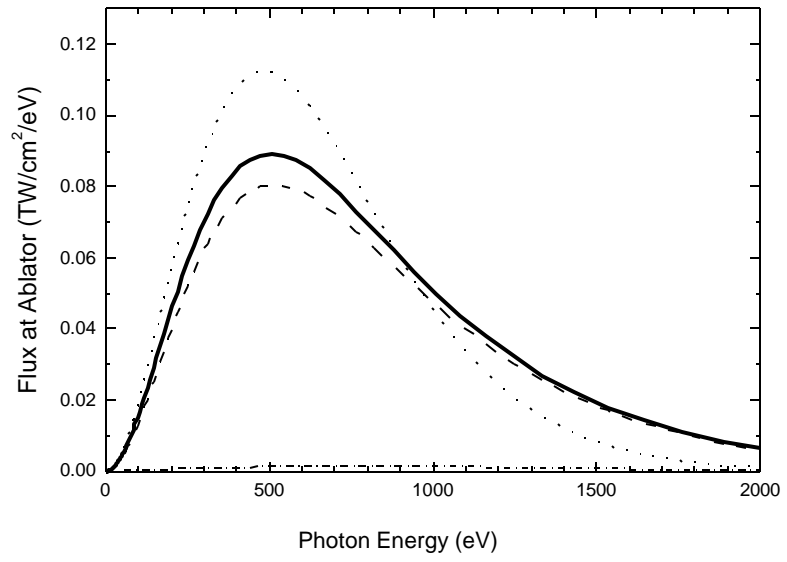




Figure 5.

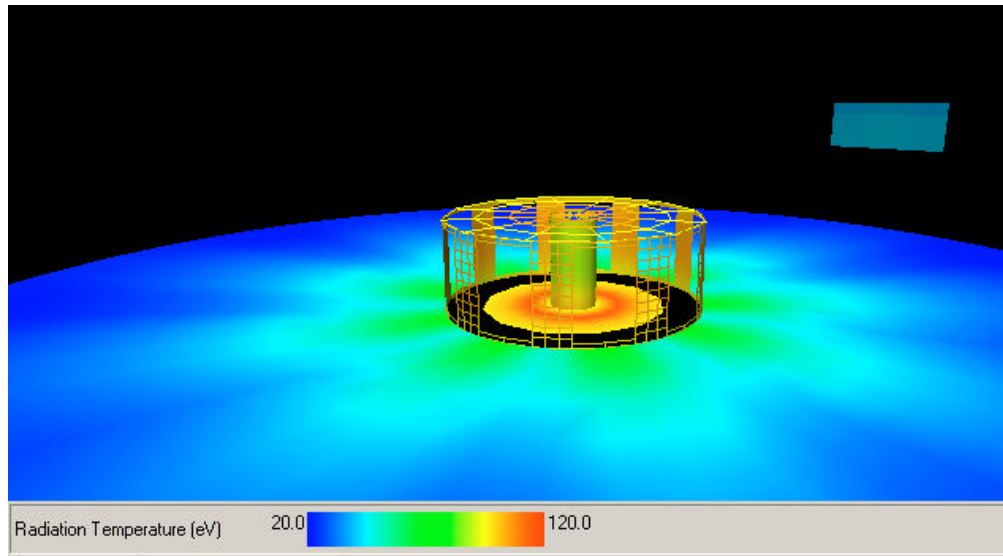


Figure 6.

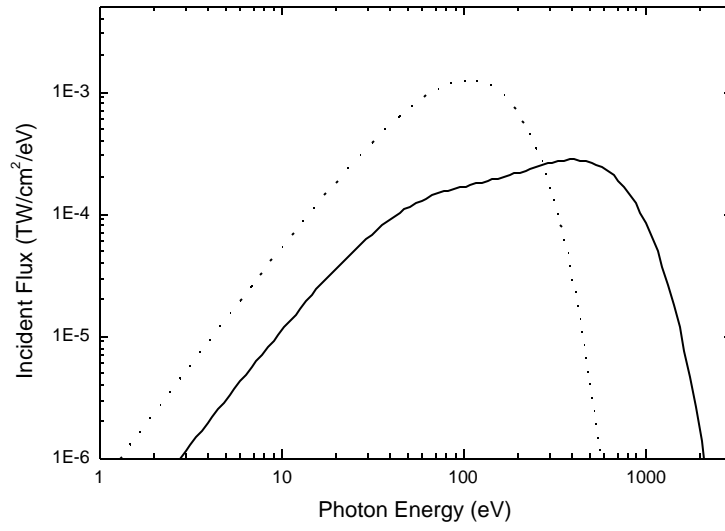


Figure A.1.

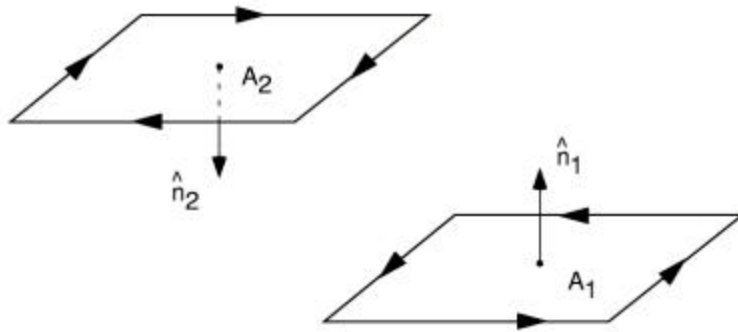


Figure A.2.

